Supporting Information

Mechanistic Insights into Defect-Governed Ion Migration and Phase Instability in Mixed-Halide Perovskites

Yueran Xiang[1], Haimeng Xin[1], Chenyu Wang[1], Fuyi Zhou[1], Hengyu Zhang[1], Pengjie Hang[1], Lingbo Xu[2], Xuegong Yu[1], Jinjing Xue[1], Deren Yang[1], and Zhenyi Ni[1,3*]

[1] State Key Laboratory of Silicon and Advanced Semiconductor Materials & School of Materials Science and Engineering & Zhejiang Provincial Key Laboratory of Optoelectronic Functional Materials and Devices, Zhejiang University, Hangzhou, Zhejiang 310027, China.

[2] Zhejiang Key Laboratory of Quantum State Control and Optical Field Manipulation, Department of Physics, Zhejiang Sci-Tech University, Hangzhou 310018, China.

[3] Shangyu Institute of Semiconductor Materials, Shaoxing 312300, China.

*Correspondence to: zyni@zju.edu.cn

Experimental section

Materials

Materials used in this work include lead (II) iodide (PbI_2, 99.999%, Sigma-Aldrich), lead (II) bromine ($PbBr_2$, 99.999% , Sigma-Aldrich), formamidinium iodide (FAI, Greatcell Solar Materials), formamidinium bromine (FABr, Greatcell Solar Materials), methylamine hydrochloride (MACl, >99.8%, Xi'an Yuri Solar Co., Ltd.), chlorobenzene (CB, 99.8%, Sigma-Aldrich), ethanol (99.8%, Sigma-Aldrich) isopropanol (IPA, 99.8%, Sigma-Aldrich), N, N-dimethylformamide (DMF, 99.9%, Sigma-Aldrich), dimethylsulfoxide (DMSO, 99.9%, Sigma-Aldrich), bathocuproine (BCP, Sigma-Aldrich), fullerene (C_{60}, 99%, Sigma-Aldrich), 1,2-ethanediamine dihydroiodide ($EDAI_2$, 99.9%, Xi'an Yuri Solar Co., Ltd.), [2-(9H-Carbazol-9-yl)ethyl]phosphonic acid (2PACz, >98%, TCI)，nickel oxide (NiO_x, 99.5%, Advanced Election Technology Co., Ltd.), All materials were used without further purification.

Device Fabrication

Patterned quartz/ITO substrates were sequentially cleaned by sonication in an aqueous detergent, deionized water, acetone, and ethanol (30 min per solvent). Following a 15-minute UV-ozone treatment, the NiO_x solution (10 mg/mL in deionized water) was spin-coated onto the substrates at 4000 rpm for 30 s and annealed at 120 ℃ in ambient air for 20 minutes. Subsequently, a 2PACz solution (2 mg/mL in ethanol) was spin-coated in a N_2 glovebox at 4000 rpm for 30 s, followed by annealing at 100 ℃ for 10 minutes.

The precursor solutions of $FAPbI_3$ and $FAPbBr_3$ were prepared separately. The $FAPbI_3$ solution was prepared by dissolving 1.45 mmol FAI, 1.6 mmol PbI_2, and 0.22 mmol MACl in 1 mL of a DMF: DMSO (4:1, v/v) mixed solvent. The $FAPbBr_3$ solution was prepared by dissolving 1.45 mmol FABr, 1.6 mmol $PbBr_2$, and 0.22 mmol MACl in 1 mL of the same solvent mixture. The $FAPb(I_{1-x}Br_x)_3$ perovskite precursor solutions were prepared by mixing the as-prepared $FAPbI_3$ and $FAPbBr_3$ precursor solutions in the required volumetric ratios. The perovskite solution was spin-coated using a two-step program: 10 s at 1000 rpm, followed by 40 s at 5000 rpm. An antisolvent (150 μL chlorobenzene, CB) was dripped onto the film 15 s before the end of the second spinning step. The wet perovskite films were then immediately transferred to a hotplate and annealed at 100 ℃ for 30 minutes. After cooling, an $EDAI_2$ solution (0.5 mg/mL in isopropanol, IPA) was spin-coated at 5000 rpm for 30 s and annealed at 100 ℃ for 5 minutes. Finally, 20 nm C_{60}, 2 nm BCP and 80 nm Ag were deposited using thermal evaporation sequentially.

Measurement

The current density-voltage test (*J-V*)

The photovoltaic performance of single-junction cells was characterized under simulated AM 1.5G illumination (100 mW/cm^2) using a solar simulator (Newport, model 94022A) calibrated with a certified silicon reference cell. Current density-voltage (*J-V*) curves were recorded with a source meter (Keithley 2400) in a nitrogen

atmosphere. An aperture mask defining an active area of 0.06 cm^2 was used during all measurements.

Structural characterization

X-ray diffraction (XRD) patterns were measured using a Bruker D8 Advance diffractometer with Cu K_α radiation (λ = 1.5406 Å) at a scanning rate of 4°/min with a step size of 0.02°. The surface morphology of the samples was characterized by field-emission scanning electron microscopy (FE-SEM, JEOL JSM-7600F). Elemental analysis was performed via energy-dispersive X-ray spectroscopy (EDS) on the same SEM platform at an acceleration voltage of 15 kV.

Transient ion drift measurement (TID)

Transient ion drift (TID) measurements were performed by applying a voltage pulse close to the built-in potential (here, 1 V for 5 s) and recording the resulting capacitance transient (ΔC) as a function of temperature. The temperature dependence of the transient reveals the activation energy of ion migration.

The calculation is based on three key assumptions: total ion concentration is conserved, the electric field varies linearly across the depletion region, and thermal diffusion of ions is negligible compared to drift. It is important to note that the linear electric field assumption represents a simplification of the actual device physics. However, this simplification does not compromise the extraction of activation energy

values, as the Arrhenius behavior governing temperature-activated ion motion remains the primary physical quantity captured by the TID analysis.[1]

The capacitance transient (ΔC) is governed exclusively by temperature, activation energy, diffusion coefficient, and mobile ion concentration as[2]:

$$C(t) = C_{\infty} + \Delta C(1 - e^{-\frac{t}{\tau}}) \quad \text{(eq.1)}$$

Where C_{∞} is the capacitance at steady-state. The τ, time constant, is given by the equation:

$$\tau = \frac{\varepsilon_0 \varepsilon k_B T}{q^2 D N_D} \quad \text{(eq.2)}$$

Where ε_0 is the vacuum permittivity, ε is the perovskite permittivity, k_B is the Boltzmann constant, T is the temperature, N_D is the electronic doping density, D is diffusion coefficient of mobile ions, the relation of D and E_a of the mobile ion can be described by the equation:

$$D = D_0 exp(-\frac{E_a}{k_B T}) \quad \text{(eq.3)}$$

The Arrhenius relationship is derived through the combination of the two equations above:

$$\ln\left(\frac{\tau}{T}\right) = \ln\left(\frac{\varepsilon_0 \varepsilon k_B}{q^2 N D_0}\right) + \frac{E_a}{k_B T} \quad \text{(eq.4)}$$

By a linear fit to $\ln(\tau/T)$-$1/T$, the slope is the activation energy of ion migration.

Furthermore, the mobile ion concentration N_{ion} can be quantified by the equation:

$$\Delta C = C_{\infty} - C_0 = C_{\infty} \frac{N_{ion}}{2N_D} \quad \text{(eq.5)}$$

Where C_0 is the initial capacitance at time t = 0 after releasing the voltage pulse.[3, 4]

To observe the effect of illumination on the ion migration properties of the mixed-halide devices, we use the following illumination conditions: a 532 nm CW laser is focussed on the considered pixel, using a 1 mW beam and a spot size of 0.06 cm^2, amounting to a power density of 16.7 mW cm^{-2}.

To rigorously decouple the contributions of anion and cation migration under illumination, we analyzed the entire TID dataset using a *global fitting procedure* (Fig. S10). This advanced method, established in the field[5], simultaneously models all capacitance transients across the full temperature range under illumination using a shared set of physically meaningful parameters, moving beyond the limitations of conventional piecewise analysis. The model employed is:

$$C(t,T) = C_{\infty}(T) + \sum_{n} C_n(T)\exp\left(\frac{-t}{P_{fit(n)}T\exp\left(\frac{E_{a(n)}}{k_B T}\right)}\right) \quad \text{(eq.6)}$$

where $C(t, T)$ is the capacitance as a function of time and temperature, $C_{\infty}(T)$ is the steady-state value of the capacitance at a certain temperature T, $\Delta C_n(T)$ is the capacitance magnitude at temperature T of the process n, $P_{fit}(n)$ is a fitted parameter for process n that depends on the diffusion coefficient, and $E_{a(n)}$ is the activation energy of the process n. $P_{fit(n)}$ and $E_{a(n)}$are global parameters fitted across all temperatures.

Mott–Schottky characterization

From Mott–Schottky characterization, the doping density N_D can be extracted directly.

$$C = A\sqrt{\frac{q\varepsilon\varepsilon_0 N_D}{2(V_{bi} - V)}} \quad \text{(eq.7)}$$

where C is capacitance, A is the device area, ε_0 is the vacuum dielectric constant, ε is the relative dielectric constant, q is the elemental charge, N_D is the doping density, V is the applied bias, and V_{bi} is the built-in potential.[6]

Thermal admittance spectroscopy measurement (TAS)

The capacitance–frequency (C–f) spectra was measured by a precision LCR meter (Keysight E4980A) at frequencies from 0.02 to 2000 kHz with a small AC voltage (20 mV). The C–f spectra was differentiated to calculate the trap density of state (tDOS) versus the frequency that represents the relative energy level (E_ω) of the trap state via the equations:

$$E_\omega = kT\ln\left(\frac{\omega_0}{\omega}\right) \quad \text{(eq.8)}$$

$$N_t = -\frac{V_{bi}\ dC\ \omega}{qAWd\omega k_B T} \quad \text{(eq.9)}$$

where ω is the angular frequency that is $2\pi f$, ω_0 is attempt-to-escape frequency, k_B is Boltzmann constant, T is the temperature, V_{bi} is the built-in potential, W is the width of depletion region and A is the active area of the device.[7]

X-ray photoelectron spectroscopy (XPS)

X-ray photoelectron spectroscopy (XPS) measurements were conducted on a Thermo Scientific ESCALAB 250xi system, which utilizes a monochromatic Al-Kα X-ray source (E = 1486.6 eV). The measurements employed a pass energy of 20 eV and an

energy step size of 0.05 eV. The binding energy scale was calibrated by setting the adventitious carbon C 1s peak to 284.8 eV for charge correction.

Steady-state photoluminescence (PL)

The steady-state photoluminescence (PL) was measured using a LuminQY (Shanghai Ideaoptics Co., Ltd) with excitation at 450 nm. Long-term light-soaking aging tests on perovskite films were conducted in a nitrogen glove box, utilizing an LED light source at 1-sun irradiation intensity, at an approximate temperature of 35 °C due to the illumination.

Supplementary Figures

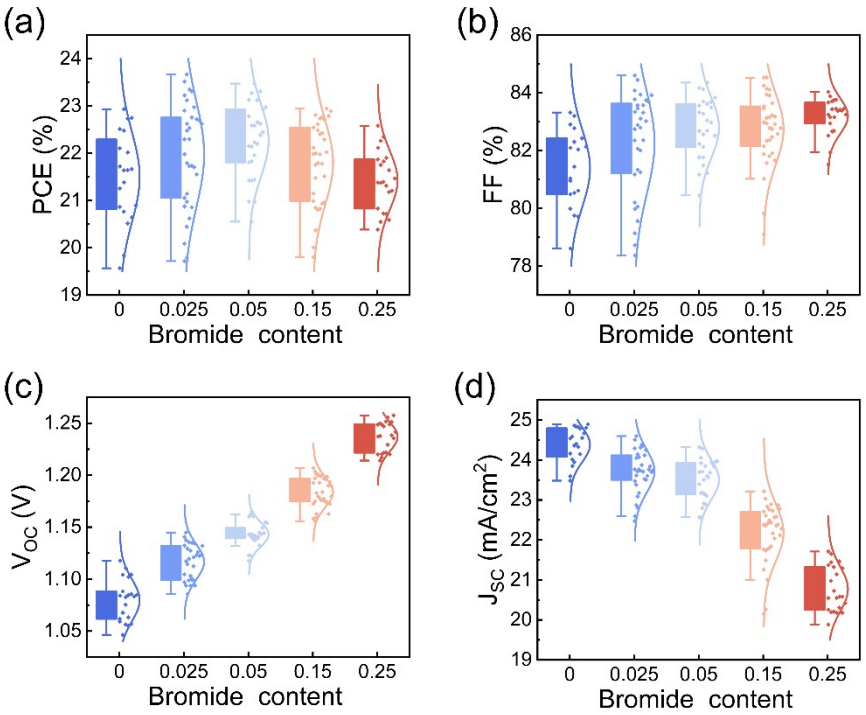

Fig. S1. Statistical distributions of photovoltaic parameters for $FAPb(I_{1-x}Br_x)_3$ solar cells with varying Br content: (a) Power conversion efficiency (PCE), (b) Fill factor (FF), (c) Open-circuit voltage (V_{OC}), (d) Short-circuit current density (J_{SC}).

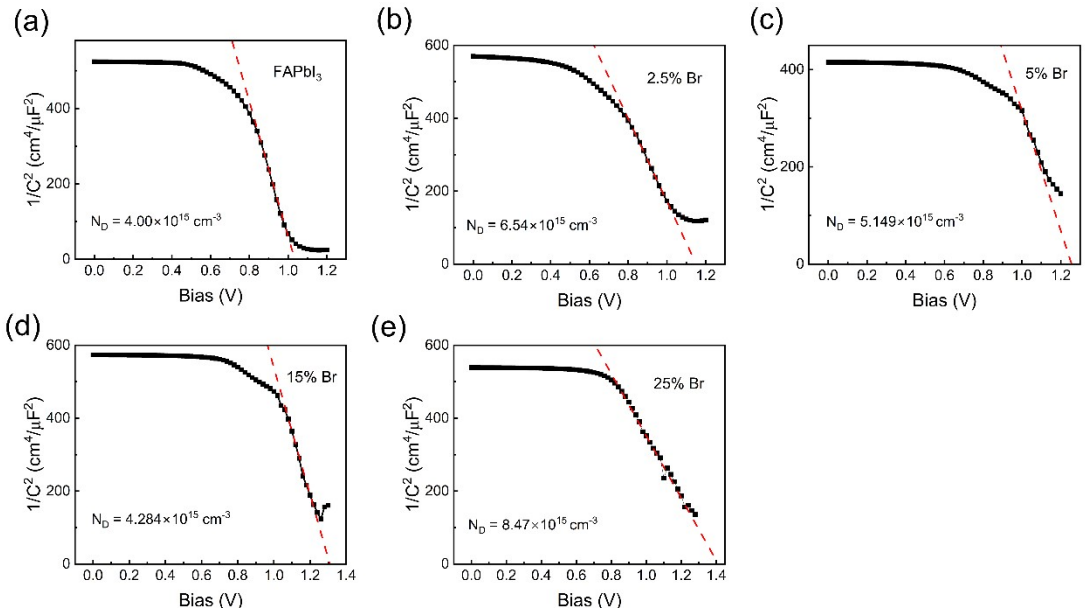

Fig. S2. Mott-Schottky plots derived from capacitance–voltage (*C-V*) measurements at 300 K on FAPb($I_{1-x}Br_x$)$_3$ devices with varying Br content, using a 10 kHz, 20 mV AC signal.

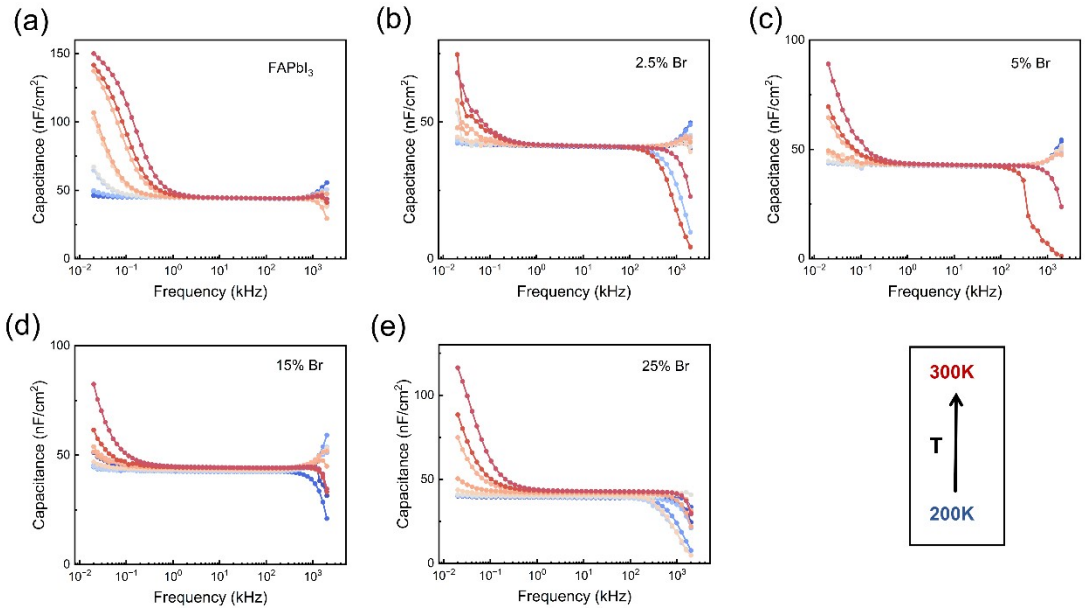

Fig. S3. Temperature-dependent impedance spectra (200 - 300 K) of $FAPb(I_{1-x}Br_x)_3$ devices, measured in the dark from 0.02 Hz to 2 MHz with an AC voltage of 20 mV.

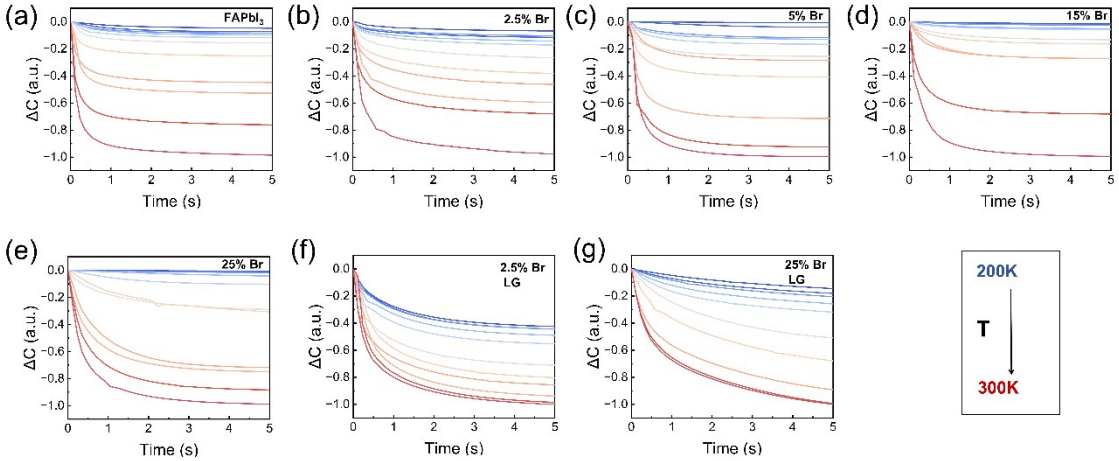

Fig. S4. Capacitance transient response ($\Delta C = C(t) - C_0$) of $FAPb(I_{1-x}Br_x)_3$ devices measured in the dark with an AC voltage of 20 mV, 10 kHz, after applying a voltage pulse of 1 V for 5 s. Samples: (a) $FAPbI_3$, (b) 2.5% Br, (c) 5% Br, (d) 15% Br, (e) 25% Br, (f) 2.5% Br with large grain size (LG) and (g) 25% Br with LG.

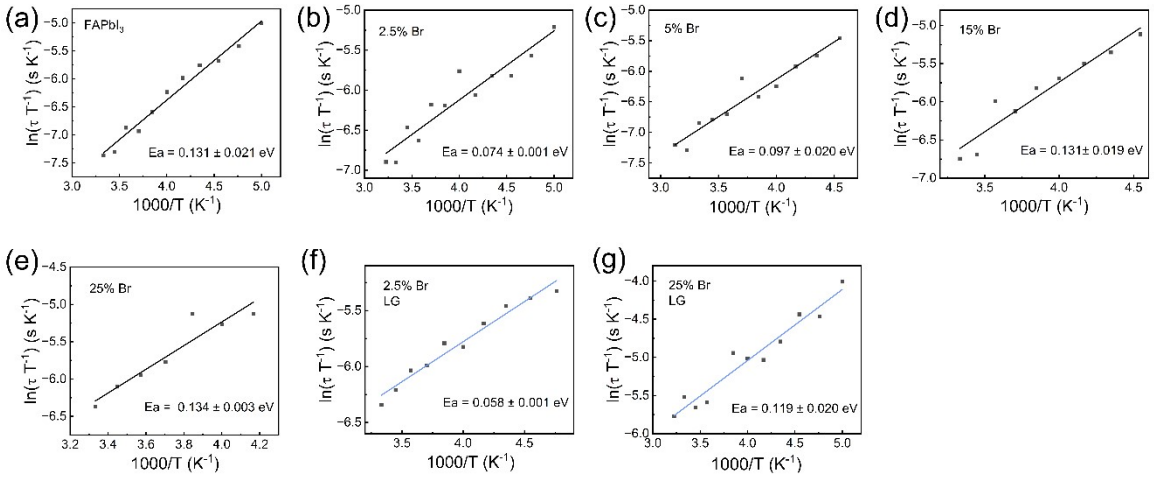

Fig. S5. Arrhenius plot of the activation energy (*E*a) derived from dark TID measurements for various $FAPb(I_{1-x}Br_x)_3$ devices: (a) $FAPbI_3$, (b) 2.5% Br, (c) 5% Br, (d) 15% Br, (e) 25% Br, (f) 2.5% Br with LG and (g) 25% Br with LG.

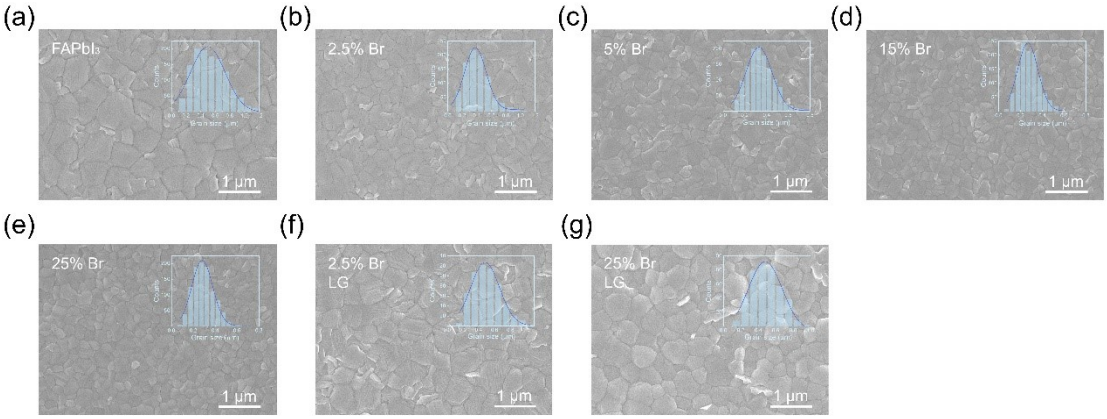

Fig. S6. Top-view SEM images of $FAPb(I_{1-x}Br_x)_3$ films with different Br content and processing conditions: (a) $FAPbI_3$, (b) 2.5% Br, (c) 5% Br, (d) 15% Br, (e) 25% Br, (f) 2.5% Br with LG and (g) 25% Br with LG.

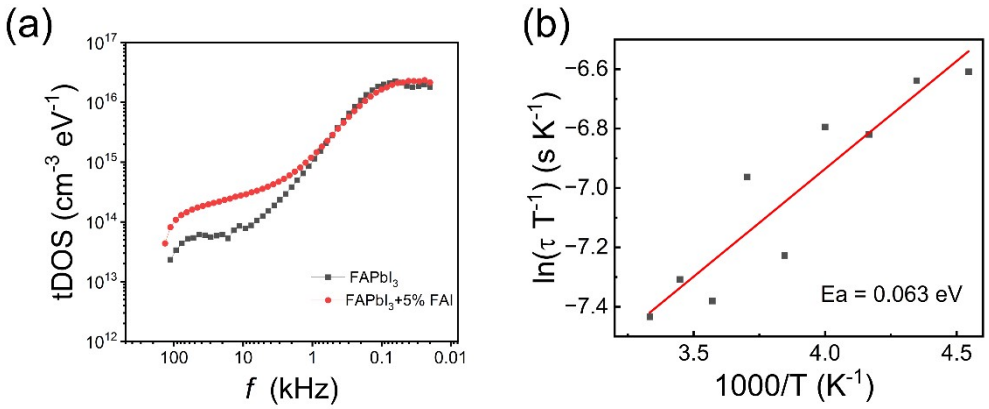

Fig. S7. (a) Comparison of tDOS spectra for PSCs based on $FAPbI_3$ with and without 5% excess FAI. (b) Arrhenius plot of the activation energy (*E*a) derived from dark TID measurements for the $FAPbI_3$ devices with 5% excess FAI.

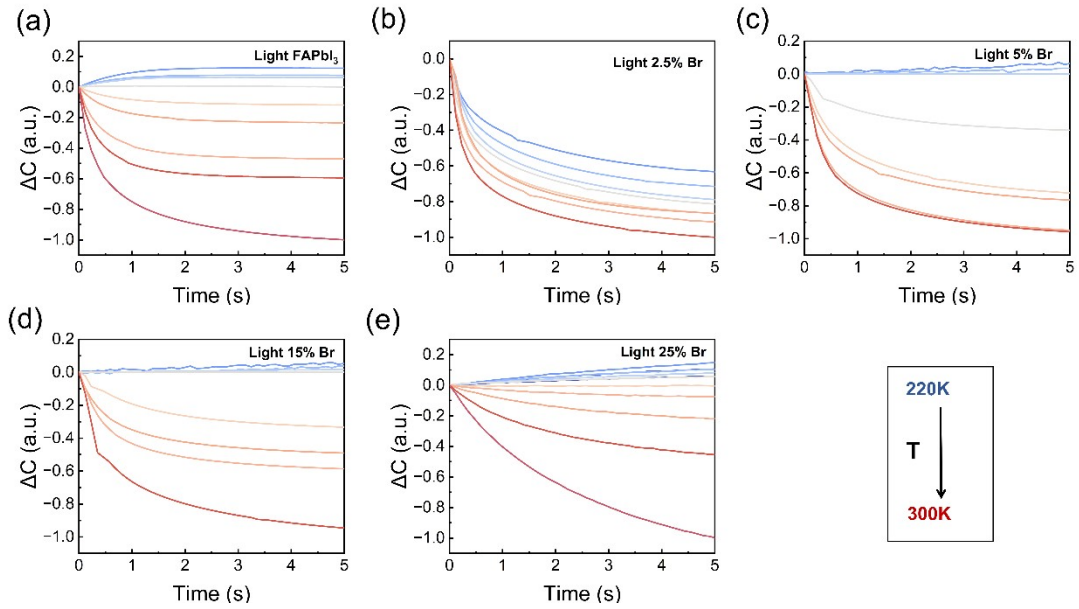

Fig. S8. Capacitance transient response ($\Delta C = C(t) - C_0$) of $FAPb(I_{1-x}Br_x)_3$ devices measured under illumination with an AC voltage of 20 mV, 10 kHz, after applying a voltage pulse of 1 V for 5 s. Illumination was provided by a 532 nm continuous-wave (CW) laser focused directly on the pixel under test.

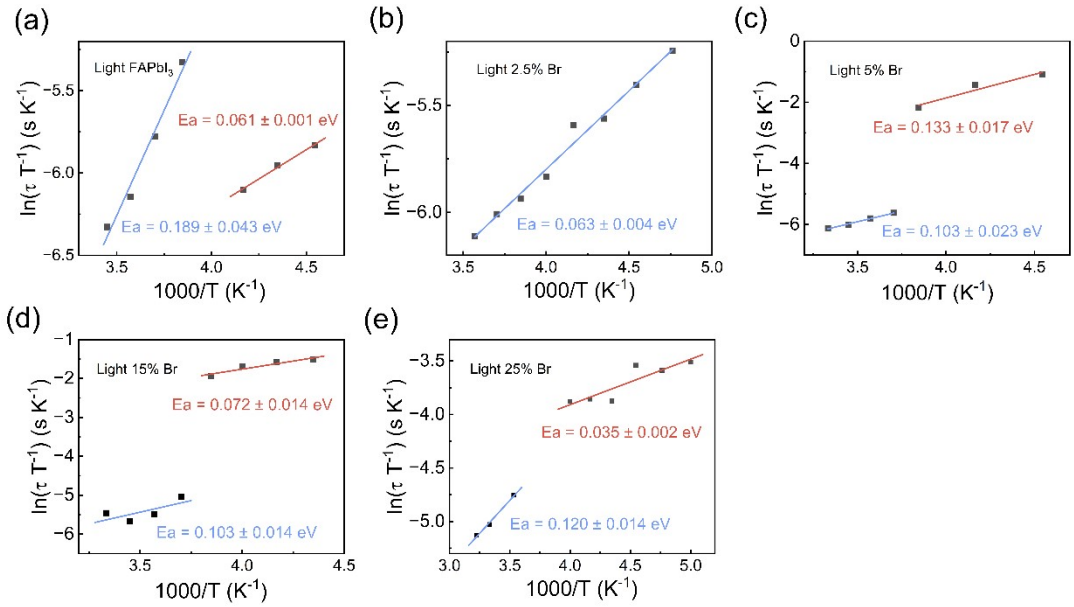

Fig. S9. Arrhenius plot of the activation energy (*E*a) derived from illuminated TID measurements for the $FAPb(I_{1-x}Br_x)_3$ devices with varying Br content: (a) $FAPbI_3$, (b) 2.5% Br, (c) 5% Br, (d) 15% Br, (e) 25% Br. Cations are represented in red and anions in blue.

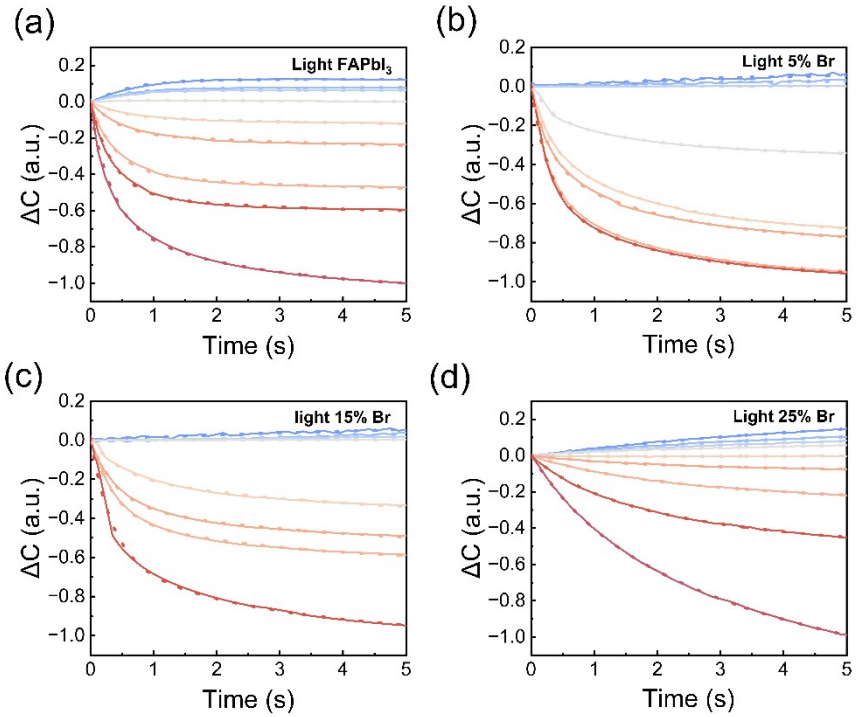

Fig. S10. Capacitance transient response of $FAPb(I_{1-x}Br_x)_3$ devices measured under illumination. The dotted lines show the global fitting results, which validate this deconvolution of ionic contributions.

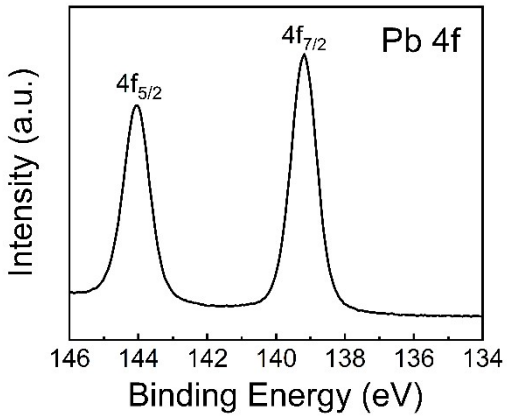

Fig. S11. The Pb 4f core-level spectrum of the perovskite film with 25% Br content after treatment under identical conditions for optical-state TID testing.

.

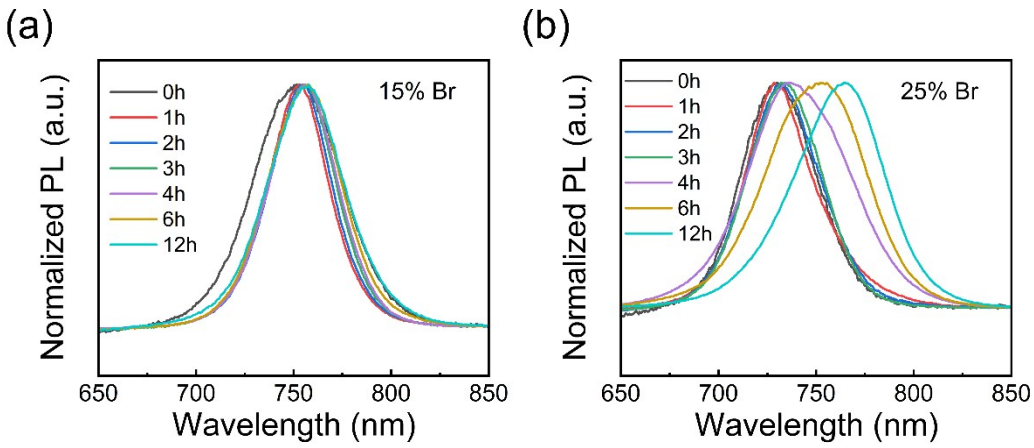

Fig. S12. Evolution of photoluminescence (PL) spectra for the $FAPb(I_{1-x}Br_x)_3$ films under continuous 1-sun AM 1.5G illumination for 12 hours. Samples with (a) 15% Br and (b) 25% Br.

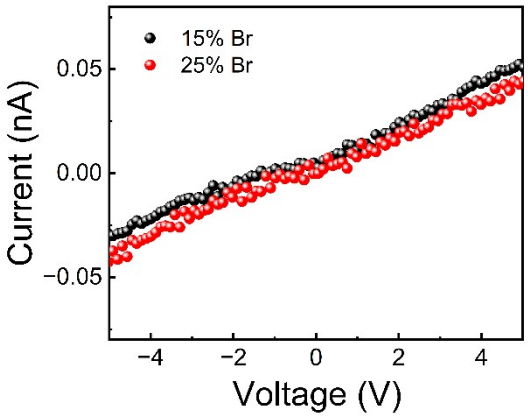

Fig. S13. Voltage - current (*V*-*I*) measurements of the Au/perovskite/Au lateral device at 300 K under dark conditions.

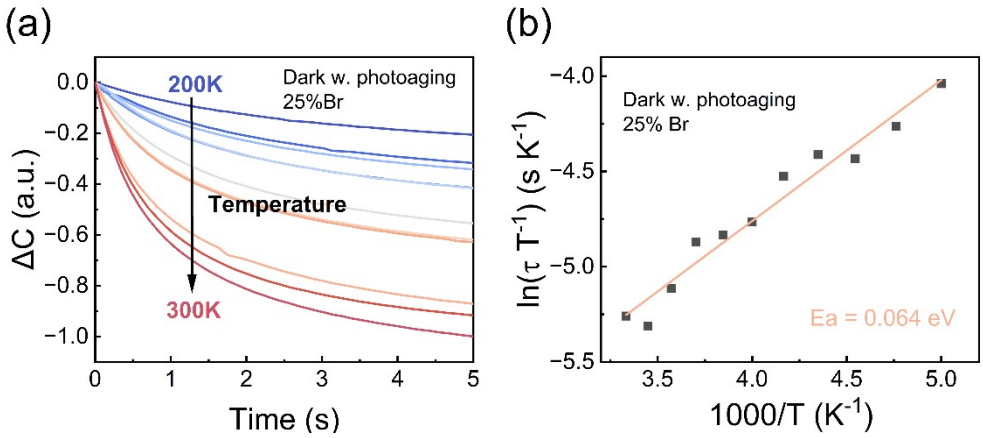

Fig. S14. Characterization of photoaged $FAPb(I_{1-x}Br_x)_3$ devices with 25% Br content (a) Capacitance transient response ($\Delta C = C(t) - C_0$) measured in the dark with an AC voltage of 20 mV, 10 kHz, after applying a voltage pulse of 1 V for 5 s. (b) Corresponding Arrhenius plot of the activation energy (*E*a) derived from the transient in (a).

Table S1 Summarized E_a in perovskite materials and devices[3, 8-15]

Composition	Ion Species	Activation energy (eV)	Technique	Reference
$MAPbI_3$	MA^+	0.46	First-principles computational	*Energy Environ. Sci.*, 2015, 8, 2118−2127
	I^-	0.08		
$MAPbBr_3$	MA^+	0.56		
	Br^-	0.09		
$MAPbI_3$	MA^+	0.84	Ab initio/DFT& chronoamperometry	*Nat. Commun.*, 2015, 6, 7497
	I^-	0.58/0.62		
$FAPbI_3$	FA^+	0.22 (<330 K)	Impedance spectroscopy	*J. Am. Chem. Soc.*, 2015, 137, 13130
		0.79 (>330 K)		
$MAPbI_3$	I^-	0.33	Temperature dependent JV curves	*Nat. Commun.*, 2016, 7, 10334
$MAPbBr_3$	Br^-	0.168		
$MAPbI_3$	I^-	0.1 ± 0.001	Temperature-dependent current density versus time	*Adv. Funct. Mater.*, 2017, 27, 1606584
	MA^+	0.41 ± 0.02		
$MAPbI_3$	MA^+	0.90 ± 0.45	Transient ion drift(TID)	*Mater. Horiz.*, 2019, 6, 1497-1503
		0.46 ± 0.25		
		0.39 ± 0.24		
	I^-	0.29 ± 0.06		
$MAPbI_3$	MA^+	0.37	Deep-level transient spectroscopy(DLTS)	*Phys. Rev. Appl.*, 2020, 13, 034018
	I^-	0.19		
$PEABr_{0.2}Cs_{0.4}MA_{0.6}PbBr_3$	Br^-	0.13 ± 0.01	Impedance spectroscopy and TID	*J. Chem. Phys.*, 2020 152, 044202
$MAPbI_3$	I^-	0.38 ± 0.03	Capacitance frequency, capacitance transient, and current transient	*ACS Energy Lett.*, 2024, 9, 5850−5858

Reference

1. T. Heiser and E. R. Weber, *Physical Review B*, 1998, **58**, 3893-3903.
2. A. Zamouche, T. Heiser and A. Mesli, *Appl. Phys. Lett.*, 1995, **66**, 631-633.
3. M. H. Futscher, J. M. Lee, L. McGovern, L. A. Muscarella, T. Y. Wang, M. I. Haider, A. Fakharuddin, L. Schmidt-Mende and B. Ehrler, *Mater. Horiz.*, 2019, **6**, 1497-1503.
4. L. McGovern, M. H. Futscher, L. A. Muscarella and B. Ehrler, *J. Phys. Chem. Lett.*, 2020, **11**, 7127-7132.
5. L. McGovern, I. Koschany, G. Grimaldi, L. A. Muscarella and B. Ehrler, *J. Phys. Chem. Lett.*, 2021, **12**, 2423-2428.
6. O. Almora, C. Aranda, E. Mas-Marzá and G. Garcia-Belmonte, *Appl. Phys. Lett.*, 2016, **109**, 173903.
7. Z. Y. Ni, H. Y. Jiao, C. B. Fei, H. Y. Gu, S. Xu, Z. H. Yu, G. Yang, Y. A. Deng, Q. Jiang, Y. Liu, Y. F. Yan and J. S. Huang, *Nat. Energy*, 2022, **7**, 65-73.
8. J. M. Azpiroz, E. Mosconi, J. Bisquert and F. De Angelis, *Energy Environ. Sci.*, 2015, **8**, 2118-2127.
9. C. Eames, J. M. Frost, P. R. F. Barnes, B. C. O'Regan, A. Walsh and M. S. Islam, *Nat. Commun.*, 2015, **6**, 7497.
10. M. Bag, L. A. Renna, R. Y. Adhikari, S. Karak, F. Liu, P. M. Lahti, T. P. Russell, M. T. Tuominen and D. Venkataraman, *Journal of the American Chemical Society*, 2015, **137**, 13130-13137.
11. S. Meloni, T. Moehl, W. Tress, M. Franckevicius, M. Saliba, Y. H. Lee, P. Gao, M. K. Nazeeruddin, S. M. Zakeeruddin, U. Rothlisberger and M. Graetzel, *Nat. Commun.*, 2016, **7**, 10334.
12. O. S. Game, G. J. Buchsbaum, Y. Y. Zhou, N. P. Padture and A. I. Kingon, *Adv. Funct. Mater.*, 2017, **27**, 1606584.
13. S. Reichert, J. Flemming, Q. Z. An, Y. Vaynzof, J. F. Pietschmann and C. Deibel, *Phys. Rev. Appl.*, 2020, **13**, 034018.
14. M. H. Futscher, M. K. Gangishetty, D. N. Congreve and B. Ehrler, *J. Chem. Phys.*, 2020, **152**, 044202.
15. M. C. Schmidt, A. O. Alvarez, J. J. de Boer, L. J. M. van de Ven and B. Ehrler, *ACS Energy Lett.*, 2024, **9**, 5850-5858.